PERFORMANCE EVALUATION OF A SURFACE-MOUNTED THERMOELECTRIC GENERATOR, DESIGNED FOR RECOVERING RESIDUAL HEAT
/
EVALUAREA PERFORMANȚEI UNUI GENERATOR TERMOELECTRIC MONTAT PE SUPRAFAȚĂ, PROIECTAT PENTRU RECUPERAREA CĂLDURII REZIDUALE

Alexandru IONESCU[1)], Florin NENCIU[1)], Mihai MATACHE[1)], Costin MIRCEA[1)], Nicolae-Valentin VLĂDUȚ[1)], Cătălin PERSU[1)], Laurențiu VLĂDUȚOIU[1)], Nicoleta VANGHELE[1)*], Robert BLEJAN[2)]

[1)] National Institute of Research – Development for Machines and Installations Designed to Agriculture and Food Industry - INMA Bucharest / Romania;

[2)] National Institute of Research & Development for Optoelectronics / INOE 2000, Subsidiary Hydraulics and Pneumatics Research Institute / IHP / Romania

Tel: +40726496637; E-mail: vanghelelrc@gmail.com

DOI: https://doi.org/10.35633/inmateh-79-110

Keywords: *energy harvesting, thermoelectric generator, waste heat recovery, carbon-neutral energy, biochar pyrolysis, Seebeck effect*

ABSTRACT

This study explores the potential of harvesting and utilizing thermoelectric energy generated during biochar production. Biochar, a carbon-rich material produced from biomass pyrolysis, offers a sustainable pathway for waste management and soil improvement. However, the biochar production process also generates significant heat, much of which remains underutilized. This research investigates the integration of thermoelectric generators (TEGs) into biochar production equipment to convert waste heat into electricity. The system's design and optimization aim to enhance energy efficiency while supporting renewable energy goals, by using the harvested energy to power up small devices, such as sensors. Experimental results demonstrate the feasibility of capturing thermal energy and converting it into usable electrical power, contributing to the overall sustainability of the process. The experimental results revealed a maximum output voltage of 1.226 V, recorded at a temperature gradient of approximately 42.0 °C, a peak power output of approximately 37.6 mW, an overall maximum temperature gradient of approximately 42.8 °C reached slightly before the voltage peak, and a cumulative harvested energy of 288.92 J. The findings also highlight key factors influencing thermoelectric conversion efficiency, including temperature gradients, TEG material properties, and system integration challenges. This approach not only mitigates energy losses but also aligns with global efforts toward carbon neutrality and resource optimization. The study underscores the dual benefit of biochar production: providing agricultural benefits while supporting energy sustainability.

REZUMAT

Acest studiu explorează potențialul de captare și utilizare a energiei termoelectrice generate în timpul producției de biochar. Biocharul, un material bogat în carbon obținut prin piroliza biomasei, oferă o cale sustenabilă pentru gestionarea deșeurilor și îmbunătățirea solului. Totuși, procesul de producere a biocharului generează, de asemenea, cantități semnificative de căldură, mare parte din aceasta rămânând nevalorificată. Această cercetare investighează integrarea generatoarelor termoelectrice (TEG) în echipamentele de producere a biocharului, pentru a transforma căldura reziduală în energie electrică. Proiectarea și optimizarea sistemului urmăresc creșterea eficienței energetice și susținerea obiectivelor de energie regenerabilă, prin utilizarea energiei recuperate pentru alimentarea unor dispozitive de mici dimensiuni, cum ar fi senzorii. Rezultatele experimentale demonstrează fezabilitatea captării energiei termice și conversiei acesteia în energie electrică utilizabilă, contribuind la sustenabilitatea generală a procesului. Rezultatele experimentale au evidențiat o tensiune maximă de ieșire de 1,226 V, înregistrată la un gradient de temperatură de aproximativ 42,0 °C, o putere maximă de aproximativ 37,6 mW, un gradient maxim general de temperatură de aproximativ 42,8 °C, atins cu puțin timp înaintea vârfului de tensiune, și o energie totală recoltată de 288,92 J. Constatările evidențiază, de asemenea, factorii cheie care influențează eficiența conversiei termoelectrice, inclusiv gradientele de temperatură, proprietățile materialelor TEG și provocările legate de integrarea sistemului. Această abordare nu doar reduce pierderile de energie, ci se aliniază și eforturilor globale pentru neutralitate carbonică și optimizarea resurselor. Studiul subliniază beneficiul dublu al producției de biochar: oferirea de avantaje agricole și susținerea sustenabilității energetice.

INTRODUCTION

In the context of increasing global energy demand and the need to reduce greenhouse gas emissions, the efficient use of available energy resources has become a critical research priority (*Cui X. et al., 2024; Moriarty P. & Honnery, D., 2016*). A significant share of the energy generated in industrial, agricultural, and biomass-processing systems is dissipated as residual heat, often without being valorized (*Jiang, Y. et al., 2024*), a situation particularly evident in processes such as biomass pyrolysis and biochar production, where high operating temperatures coexist with relatively low overall energy efficiency (*Champier D., 2017*); Seebeck-based recovery from biomass carbonization heat has recently been explored in simulation (*Badaka H. K. & Morega A. M., 2024*). In power stations, for example, approximately two-thirds of the energy produced is lost as waste heat, mainly discharged through cooling towers, since most electricity generation relies on gas- or steam-powered turbine systems in which fuel combustion is first converted into mechanical energy and only subsequently into electricity (*Sanin-Villa D., 2022*). As a result, only about one-third of the energy released from the fuel reaches the power lines leaving the plant.

Several technologies exist for recovering this thermal energy, including Organic Rankine Cycles (ORC), turbo-compounding, and thermoelectric generators (TEGs). Among these, TEGs are a promising solution for the direct conversion of waste heat into electricity. Based on the Seebeck effect, they enable solid-state energy conversion without moving parts, offering high reliability, low maintenance requirements, and scalability (*Ridwan M., 2025*), and have been increasingly investigated for waste-heat recovery from internal combustion engines, industrial processes, and biomass-based systems (*Williams, N. P. et al., 2022*), including automotive exhaust-heat recovery, where structural design and optimization remain active research topics (*Wang Y. et al., 2025*). Thermoelectric recovery from such systems typically relies on arrays of thermoelectric modules (TEMs) applied to surfaces with non-uniform temperature distributions, reducing fuel consumption and pollutant emissions in the process (*Săvescu C. et al., 2025*).

The Seebeck effect arises from the diffusion of charge carriers along a temperature gradient in a conductor or semiconductor, generating a potential difference between the hot and cold sides; the sign of this potential- and of the corresponding Seebeck coefficient identifies the material as p-type (positive) or n-type (negative) (*Quan R. et al., 2020*). The Seebeck coefficient quantifies the ratio between the induced voltage and the applied temperature gradient, and is obtained using a thermoelectric circuit formed of two dissimilar materials, typically two semiconductors with opposite-sign coefficients, joined at junctions held at different temperatures (*Deng Y. et al., 2022*). Materials with a high Seebeck coefficient are the most efficient at converting thermal energy into electricity; the effect underlies applications ranging from thermoelectric generators and thermocouple temperature sensors to wearable devices that harvest body heat.

Despite these advantages, wider adoption of thermoelectric systems remains limited by relatively low conversion efficiencies and by challenges related to thermal integration (*Liu Z. et al., 2023*). TEG performance depends not only on the intrinsic properties of the thermoelectric materials but also on external factors such as the temperature gradient, heat-transfer conditions, and the quality of thermal contact between the heat source and the modules (*Ciupercă R. et al., 2022*). Surface-mounted configurations are particularly sensitive to heat-transfer effectiveness across multiple interfaces, where thermal resistances and contact imperfections can substantially reduce the achievable temperature difference (ΔT) and, consequently, the electrical output (*Mastrullo R. et al., 2019*). The complementary Peltier effect, in which an electric current passed through the junction of two dissimilar materials causes heat to be absorbed at one junction and released at the other, governs the reverse operating mode of the same devices, used for active cooling, and reflects the same carrier-transport mechanism that underlies Seebeck-based power generation (*Chelladorai P. et al., 2024; Maican E., 2015*).

Fig. 1 - Seebeck effect *(Kim M., et al., 2025)* **Fig. 2 - Peltier effect** *(Kim M., et al., 2025)*

MATERIALS AND METHODS

Thermoelectric generators (TEG)

A thermoelectric generator (TEG) directly converts heat into electrical energy through the Seebeck effect: when a temperature difference is applied across a conductive or semiconductive material, charge carriers diffuse from the hot end to the cold end, producing an electric current. A practical TEG is built from multiple thermocouples, each an n-type and a p-type semiconductor pair, connected electrically in series and thermally in parallel; the conversion efficiency depends on the thermoelectric material used and is quantified by the dimensionless figure of merit (ZT), which combines electrical conductivity, the Seebeck coefficient, absolute temperature and thermal conductivity (*Ridwan M., 2025*).

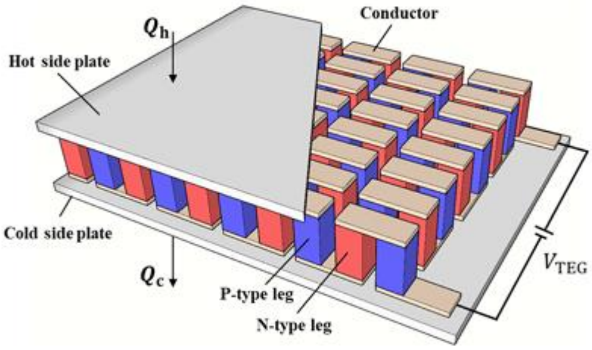

Fig. 3 - Graphic representation of a thermoelectric generator *(Yaman K., et al., 2025)*

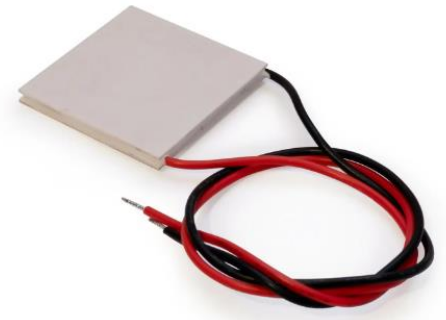

Fig. 4 - Thermoelectric generator module *(Iavnic T., et al., 2024)*

Bismuth telluride (Bi_2Te_3), the active material in the TEC1-12706 Peltier modules used in this study, is among the most widely used thermoelectric materials for near-room-temperature applications (typically 200-300 °C), owing to its favorable electrical conductivity and Seebeck coefficient and its correspondingly high figure of merit (ZT) at low-to-medium temperatures; it is likewise the basis for the reverse (cooling) operating mode of the same devices in thermoelectric refrigeration.

- **Heat source**

The biochar production equipment (Fig. 7) generates high temperatures during the pyrolysis process. The external surfaces of the equipment have been identified as a consistent source of residual heat, making them ideal for mounting Peltier modules.

Although thermally insulated, the heat generated by the six 2000 W heating elements is sufficient for four series-connected Peltier modules to generate a significant electric potential.

Fig. 5 - Bismuth telluride in natural form *(Hqgraphene.com)*

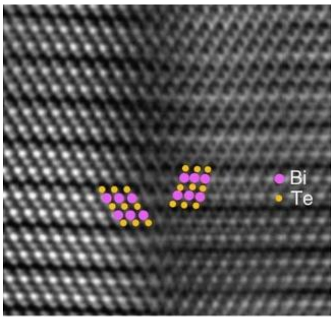

Fig. 6 - Bismuth telluride under microscope *(Hqgraphene.com)*

Fig. 7 - Biochar production equipment

- **TEG modules**

The core of the system comprises four TEC1-12706 modules. While these are primarily designed as Peltier modules for thermoelectric cooling and heating, they can be repurposed as thermoelectric generators (TEGs) when subjected to a temperature gradient. In this configuration, they convert heat into electrical energy through the Seebeck effect. To maximize the voltage output from the TEGs, the four modules are connected in series. This configuration ensures that the voltage generated by each module adds up, resulting in a combined output equal to the sum of individual module voltages. This is particularly advantageous when the application requires higher voltages to power downstream electronics or charge batteries.

For a better cooling distribution on the cold side of the generator, a heat sink was mounted on each of the four modules with thermal paste. (Fig. 8)

Being a low-powered application, it is important to minimize the voltage drop as much as possible. The voltage drop across conductive materials is governed by Ohm's law:

$$U = I \cdot R \tag{1}$$

where U is the voltage drop, I is the current, and R is the resistance of the wire. The resistance (R) of a wire is proportional to its length (L) and resistivity (ρ) and inversely proportional to its cross-sectional area (S):

$$R = \rho \cdot \frac{L}{S} \tag{2}$$

To minimize the resistance of the wiring used with thermoelectric generator (TEG) modules and consequently reduce the voltage drop, the wire length (L) was minimized in this design. This approach ensures that the electrical energy generated by the TEG modules is efficiently transferred to the load or storage system. Shortening the wire length not only reduces resistive losses but also minimizes the thermal resistance introduced by longer wires, which can interfere with the thermal gradient for TEG operation. This optimization step is particularly critical in low-voltage systems, where even minor losses can significantly impact overall performance.

Before conducting the actual experiments, preliminary tests were performed to determine the correct polarity of the thermoelectric generator (TEG) modules and to confirm their functionality based on the Seebeck effect. These tests involved applying a temperature gradient across the module surfaces.

To simulate a temperature differential, heat was applied to the hot side of the TEG module using a handheld lighter, while ice was placed on the cold side. This setup ensured a significant thermal gradient necessary to generate an electromotive force. Using a multimeter, the output voltage and polarity were measured to verify the module's orientation and ensure proper connectivity for subsequent testing. The results confirmed the expected behavior, with the TEG generating a voltage consistent with the Seebeck effect and the designated polarity. This step was a qualitative orientation check preceding the formal experimental campaign described in the following sections, and is reported here only as such, not as part of the formal measurement procedure.

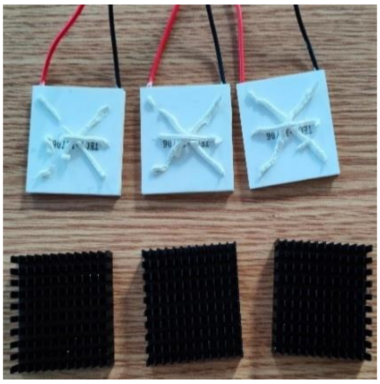

Fig. 8 - Heat-sink mounting using thermal paste

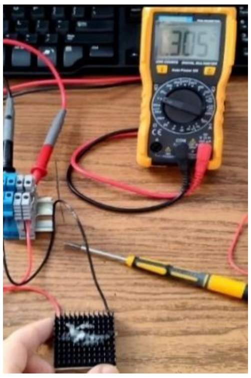

Fig. 9 - Applying ice on the cold side

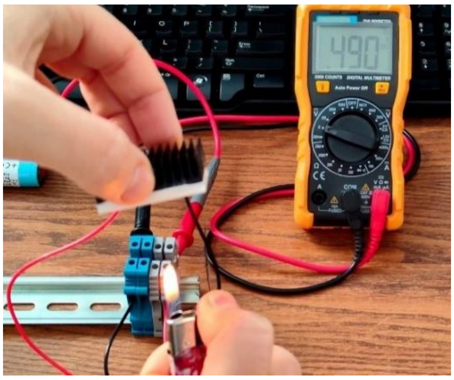

Fig. 10 - Applying high temperature on hot side

For ensuring an efficient and uniform heat distribution across the hot-side surfaces of the Peltier modules, they were mounted on a copper plate, due to its superior thermal conductivity properties. Subsequently, the assembled structure was attached to the equipment using a thermally conductive double-sided adhesive tape, providing both mechanical stability and adequate thermal contact. In order to enhance thermal dissipation and reduce the temperature at the cold junction, the setup utilized four heat sinks, each with dimensions of 40x40 mm.

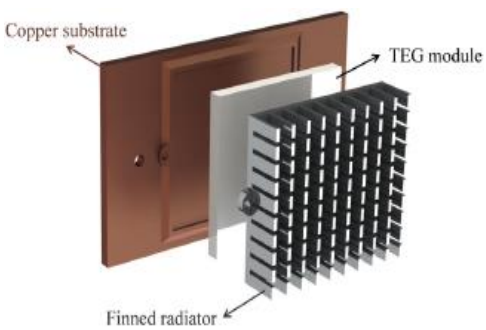

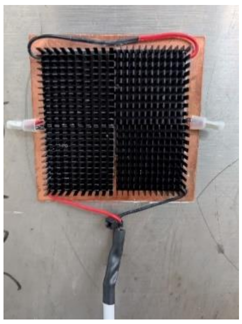

Figure 11. Geometric model of a TEG module with a finned heat sink and copper plate
(Jiang, Y. et. al., 2024)

Figure 12. TEG modules setup

Other instrumentation used

The output voltage and current supplied to the resistive load (Fig. 16) were measured with a PANCONTROL PAN Profimeter digital multimeter (CAT III 600 V), with a DC voltage range of 0.1 mV–600 V and a manufacturer- specified accuracy of 0.7%–4.0% depending on range and function.

Thermal measurements were performed using a UNI-T UTi32 thermal imaging camera. The device operates over a temperature measurement range of −20 °C to 1000 °C and features an infrared (IR) resolution of 32 × 32 pixels. The thermal images were displayed on a 2.4-inch IPS screen with a resolution of 480 × 320 pixels. In addition, the integrated digital camera provides visible-light images at a resolution of 640 × 480 pixels. The camera supports three visualization modes: thermal, visible, and fusion, allowing thermal data to be analyzed alongside conventional imagery. According to the manufacturer's specifications, the instrument has a stated temperature-measurement accuracy of ±2 °C or ±2%, whichever is greater, and a thermal sensitivity (NETD) of 0.15 °C.

Temperature regulation was performed using a Gefran 650 PID temperature controller, a compact 1/16 DIN process controller designed for accurate and stable thermal regulation in industrial applications. The controller has a 48 × 48 mm front-panel format and an approximate depth of 80 mm. Its universal main input can be configured for different temperature sensors, including J, K, R, S, T, C and D thermocouples, as well as PT100 and JPT100 resistance temperature detectors (RTDs). Linear input signals of 0–60 mV, 0–1 V, 0–5 V, 0–10 V and 0/4–20 mA are also supported.

Temperature at the module hot side was sensed with a Gefran TC8-D-1-K thermocouple (Type K), connected to the Gefran 650 controller, with a manufacturer-stated tolerance of IEC 60584-2 Class 2: ±2.5 °C for −40...+333 °C, or ±0.0075×|t| for t > 333 °C (i.e., approximately ±3 °C at the ~400 °C internal operating temperature reached in this study).

The 10 Ω load resistor was a general-purpose commercial resistor with a typical tolerance of ±5%, as manufacturer-specific tolerance data were not available for this component.

Methodology

The measurements were conducted in Bucharest on December 11, 2025. Ambient temperature data were obtained from the website weatherspark.com. The measurements were carried out over a period of 335 minutes, from 9:00 a.m. to approximately 3:30 p.m., with ambient temperatures ranging between 3°C and 12°C. In addition, temperature and output voltage measurements were recorded at 5-minute intervals throughout the duration of the experiment.

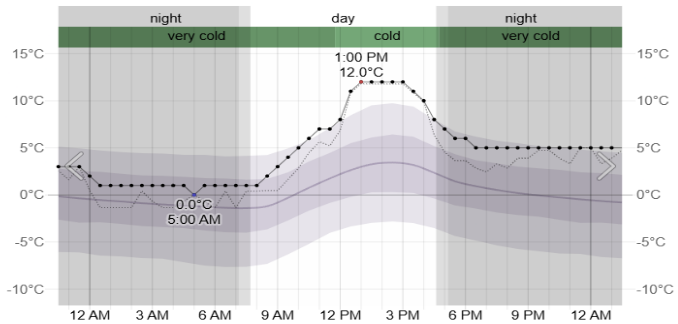

Fig. 13 - Ambient temperatures in Bucharest, 11 Dec 2025 *(Weatherspark.com)*

For the experimental determination of the electrical parameters (current, and output power), a resistive load of 10 Ω was connected across the terminals of the thermoelectric modules. The selection of this load value was based on the maximum power transfer principle, which states that the power delivered to the load is maximized when the load resistance is approximately equal to the internal resistance of the source.

Each thermoelectric module exhibits an internal electrical resistance of approximately 2.5 Ω. With the four modules connected in series, as described above, the equivalent internal resistance of the source is 4 × 2.5 Ω = 10 Ω, which matches the selected load resistance exactly. Therefore, the use of a 10 Ω load closely satisfies the impedance matching condition, enabling an accurate experimental assessment of the maximum extractable power from the system; this equivalence between the source and load resistance is also what justifies halving the total output voltage in Eq. (3) below.

$$V_{load} = \frac{V_{out}}{2} \quad (3)$$
$$I = \frac{V_{load}}{R_L} \quad (4)$$
$$P = V_{load} \cdot I = \frac{V_{load}^2}{R_L} \quad (5)$$
$$\eta = \frac{P}{Q} \quad (6)$$

where:

V_{load} – voltage measured across the load resistor [V]

I – electrical current flowing through the circuit [A]

P – electrical power delivered to the load [W]

P_{avg} – average electrical power delivered to the load [W]

η – yield, expressed here as a conversion ratio relative to the fixed reference power Q_{ref} = 180 W (see Results), rather than a directly measured thermoelectric conversion efficiency [%]

The average electrical power obtained during the experimental campaign was 14.37432 mW. The total duration of the experiment was 335 minutes, corresponding to 20,100 seconds. Based on these values, the total electrical energy generated by the system was calculated as the product of average power and time.

$$E \approx P_{avg} \cdot t \approx 0.01437432 \cdot 20100 \approx 288.92 \text{ [J]} \quad (7)$$

where:

E – electrical energy produced by the system [J]

Theoretical model

The electrical voltage generated by the thermoelectric modules is governed by the Seebeck effect, which establishes a direct proportionality between the generated voltage and the temperature difference across the module.

$$V = \alpha \cdot \Delta T + b \quad (8)$$

where:

V - output voltage [V];

α - Seebeck coefficient [V/K];

ΔT - temperature difference across the module [K].

The thermoelectric modules were mounted on the external surface of the biochar production equipment. Therefore, the temperature difference was defined as:

$$\Delta T = T_{hot} - T_{cold} \quad (9)$$

To determine the temperatures at the ceramic surfaces of the TEGs (Thot and Tcold), it had to be accounted the fact that heat doesn't transfer perfectly from the heat source to the modules as there is thermal friction (thermal resistance) in the copper plate and especially in the thermally conductive tape used.

When heat flows through any material, it loses "pressure" (temperature). The temperature at the actual Peltier junction is always lower than the source and higher than the ambient air.

$$T_{hot} = T_{ext} - (Q \cdot R_{hot}) \quad (10)$$
$$T_{cold} = T_{amb} + (Q \cdot R_{cold}) \quad (11)$$
$$Q = \frac{T_{top} - T_{bottom}}{R_{th}} \quad (12)$$

where:

Q - heat flow [W]

R - thermal resistance [K/W]

T_{top} – temperature on the top of a material [°C]

T_{bottom} – temperature on the bottom of a material [°C]

- **Hot side thermal resistance model**

To determine the temperature drop between the measured external temperature, *T*ext, and the actual hot-side surface temperature of the TEG, *T*hot, Fourier's law of heat conduction and a thermal-resistance model were applied.

$$R_{th} = \frac{L}{k \cdot A} \quad (13)$$

where:

L – thickness of the material (m)

k – thermal conductivity (W/mK)

A – surface area (m²)

$$T_{drop} = Q \cdot R_{th} \quad (14)$$

where:

T_{drop} – Temperature drop across a layer [°C]

The thickness of the copper plate is 1mm, while the other dimensions are 40x40 mm, it results:

$$R_{copper} = \frac{L_{copper}}{k_{copper} \cdot A_{copper}} = \frac{0.001}{401 \cdot 0.0064} \approx 0.00039 \text{ [K/W]} \quad (15)$$

It means that the thermal resistance of the copper plate is negligible, the copper plate itself barely causing any temperature drop (less than 0.1°C).

As for the thermally conductive tape, its thickness was measured as 0.2 mm, while the dimensions are 40x40 mm. Therefore:

$$R_{band} = \frac{L_{band}}{k_{band} \cdot A_{band}} = \frac{0.0002}{1.5 \cdot 0.0064} \approx 0.02083 \text{ [K/W]} \quad (16)$$

- **Cold side thermal resistance model**

Although copper has high thermal conductivity, air has much lower thermal conductivity. As a result, heat dissipation from the heat sinks to the surrounding air is limited, causing the cold side of the TEG module to remain warmer than the ambient temperature.

The effective cold side temperature T_{cold} is calculated by adding the temperature loss factors to the ambient air temperature:

$$T_{cold} = T_{amb} + T_{convective} + T_{conduction} \quad (17)$$

The total cold side resistance (R_{cold}), consists of three components:

- Interface Resistance (R_{int}) - thermal resistance at the contact interface between the TEG module and the heat sink.
- Conduction Resistance ($R_{conduction}$) - thermal resistance associated with heat conduction through the aluminum base of the heat sink.
- Convective Resistance ($R_{convective}$) - thermal resistance associated with heat transfer from the heat-sink fins to the surrounding air; this component typically accounts for the largest temperature drop.

$$R_{convective} = \frac{1}{h \cdot A} = \frac{1}{50 \cdot 0.0064} \approx 3.125 \text{ [K/W]} \quad (18)$$

The convective heat-transfer coefficient adopted in Eq.(18) (h = 50 W/(m²K)) reflects a natural-convection regime for the finned heat sinks used, since no forced-air cooling (fan or blower) was applied during testing.

The other two terms in Eq. (19) — the interface resistance between the TEG module and the heat sink, associated with the thin layer of thermal paste, and the conduction resistance through the thin aluminum base of the heat sink — are, by the same reasoning applied to the copper plate on the hot side in Eq. (15), several orders of magnitude smaller than the convective resistance calculated in Eq. (18). They were therefore neglected. Consequently, the cold-side temperature rise is dominated by the convective resistance, with $R_{convective}$ ≈ 3.125 K/W.

The heat flow, Q, rejected at the cold side consists of the heat transferred from the hot side together with the internally generated Joule heat:

$$T_{rise} = Q_{total} \cdot (R_{int} + R_{conduction} + R_{convection}) \quad (19)$$

Because the convective thermal resistance of the heat sink $R_{convection}$ is determined primarily by the heat-sink geometry and airflow conditions, a higher heat flow results in a larger temperature difference across the cold-side thermal resistance.

The Seebeck coefficient was determined using linear regression applied to the experimental dataset, according to the relation:

$$\alpha = \frac{V_{out}}{\Delta T} \quad (20)$$

Since the experiment was conducted using 4 modules mounted in series:

$$V_{out} = 4 \cdot \alpha \cdot \Delta T \quad (21)$$

The linear regression fitted to the full V_{out} versus ΔT dataset (Figure 21) gives a slope of 0.0293 V/°C for the four-module series, corresponding to a per-module Seebeck coefficient of:

$$\alpha_{module} = \frac{0.0293}{4} = 0.00733 \text{ [V/K]} \quad (22)$$

As a consistency check, the Seebeck coefficient was also estimated from a single stable data point near the plateau, where the open-circuit output voltage was V_{out} = 1.226 V and ΔT ≈ 42.0 °C.

$$\alpha_{module} = \frac{V_{out}}{4 \cdot \Delta T} = \frac{1.226}{4 \cdot 42.0} = 0.00729 \text{ [V/K]} \tag{23}$$

where: α - the effective Seebeck coefficient of the thermoelectric module under real operating conditions [V/K]

ΔT - temperature difference between the hot and cold side of the module [°C]

V_{out} - voltage measured at the corresponding temperature difference ΔT [V]

The close agreement between the regression-based estimate (0.00733 V/K) and the single-point value (0.00729 V/K) confirms the consistency of the Seebeck coefficient obtained under real operating conditions, and both are in line with the expected performance of commercial thermoelectric modules operating under non-ideal thermal conditions. As shown in Figures 21 and 23, the heating and cooling phases form two visibly distinct branches around this regression line, a hysteresis attributable to the thermal inertia of the system discussed above; the reported slope represents an average across both branches rather than a single-valued instantaneous relationship.

RESULTS

The biochar production unit, acting as the thermal source, reached the target internal temperature of 400 °C in approximately one hour. This temperature was maintained for a duration of about two hours, after which a gradual decrease was observed.

A pronounced thermal inertia of the system was identified. While the internal temperature attained its maximum value within the first hour, the external surface temperature exhibited a delayed response, reaching a peak of 71 °C after approximately three hours from the start of the process. This behavior highlights the transient heat transfer dynamics and the thermal buffering capacity of the system.

Fig. 14 - Measurement of the equipment surface temperature

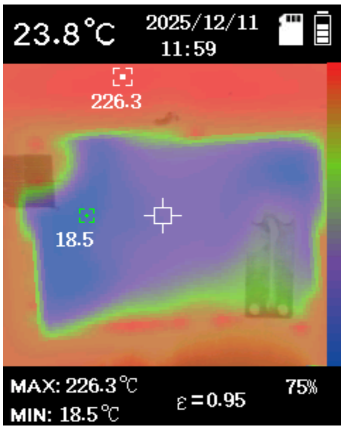

Fig. 15 - UNI-T thermal camera screenshot

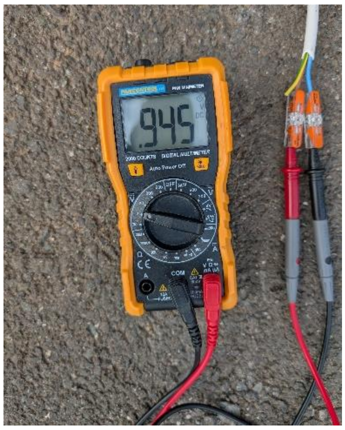

Fig. 16 - Measuring the output voltage

Although the theoretical model predicts a linear relationship between output voltage and temperature difference, the experimental results show deviations from ideal linearity. These deviations may be attributed to several factors, including thermal contact resistance between the module and the equipment surface, insufficient heat dissipation from the cold side, transient thermal conditions during measurement, and nonuniform temperature distribution within the module. These values indicate that the system is suitable for low-power applications such as environmental monitoring or autonomous sensing systems.

The experimental measurements performed over a total duration of 335 minutes highlight the temporal evolution of the thermal regime of the biochar reactor and its direct influence on thermoelectric energy generation.

- **Thermal evolution of the system**

The internal temperature of the heat source exhibited a rapid increase during the initial phase, rising from near-ambient values to approximately 400 °C within the first 60–65 minutes. After reaching this peak, the system maintained a quasi-steady thermal plateau at ~400 °C for a significant duration (approximately 65 to 190 minutes), followed by a gradual cooling phase.

In contrast, the external temperature of the heat source and the temperatures measured at the thermoelectric module interfaces (hot and cold sides) showed a delayed and attenuated response. The hot-side temperature increased progressively from ~5.8 °C to a maximum of approximately 62.4 °C, while the cold-side temperature rose from ~3.5 °C to about 20.6 °C. This resulted in a maximum recorded temperature difference (ΔT) of approximately 42.8 °C.

The data clearly indicate the presence of thermal gradients and heat transfer limitations between the reactor core and the thermoelectric modules, as the external and interface temperatures remained significantly lower than the internal reactor temperature throughout the experiment.

- **Voltage generation and correlation with temperature gradient**

The electrical output of the thermoelectric modules followed the evolution of the temperature gradient across their surfaces. At low ΔT values (approximately 2–3 °C), the generated voltage was minimal (~0.02 V). As ΔT increased, the output voltage rose steadily, reaching a maximum value of 1.226 V at ΔT ≈ 42 °C.

During the steady-state thermal regime (approximately 160–190 minutes), both ΔT and voltage output stabilized, with voltage values consistently around 1.20–1.22 V. This indicates a strong correlation between thermal stability and consistent electrical generation.

Following the decline in reactor temperature, both ΔT and output voltage decreased proportionally, confirming the direct dependence of thermoelectric performance on the available temperature gradient.

- **Electrical performance under load**

The electrical characterization of the system using a 10 Ω resistive load provided insight into the practical energy harvesting capability. The measured current increased with ΔT, ranging from approximately 1 mA at low temperature differences to 61.3 mA at peak conditions.

The corresponding electrical power output reached a maximum value of approximately 37.6 mW at ΔT ≈ 42 °C. At intermediate conditions (ΔT ≈ 26.3 °C), the system produced around 10.8 mW, while at low ΔT values (~2–3 °C), the power output was negligible (~0.01 mW).

These results confirm that the usable electrical power is highly sensitive to the temperature gradient and increases nonlinearly with ΔT.

- **Energy conversion efficiency**

The calculated P/Q_{ref} conversion ratio (yield) remained low throughout the experiment, with values ranging from 0.0001% at minimal ΔT to a maximum of approximately 0.021% at peak operating conditions. Even under stable high-temperature conditions, this ratio did not exceed that value; as explained above, it is referred to the fixed reference power Q_{ref} = 180 W rather than to a per-point modelled heat flow, so it should not be interpreted as a directly measured thermoelectric conversion efficiency.

This limited efficiency reflects both the inherent constraints of thermoelectric conversion at relatively low temperature gradients and the thermal losses occurring within the system.

- **Observed thermal effects influencing performance**

The experimental data reveal several important physical phenomena affecting system performance:

- ✓ A temperature lag between the internal reactor temperature and the thermoelectric module temperatures, indicating significant thermal inertia.
- ✓ A reduced effective ΔT across the modules compared to the available thermal potential, suggesting heat transfer limitations.
- ✓ A gradual rather than instantaneous response of voltage output to temperature changes, further supporting the presence of thermal inertia in the system.

Additionally, the relatively low hot-side temperatures compared to the reactor interior suggest the presence of thermal resistance along the heat transfer path, which limits the effective utilization of the available heat.

Table 1

Summary of key operating points across the thermal cycle

Time point	T_ext (°C)	T_int (°C)	T_hot (°C)	T_cold (°C)	ΔT (°C)	V_out (V)	I (mA)	P (mW)	η (%)	Qref (W)
Start (t = 5 min)	6.3	8.3	5.8	3.5	2.3	0.020	1.0	0.010	0.0000056	180
Plateau onset (t = 65 min)	27.5	401.0	24.1	8.4	15.8	0.359	17.95	3.222	0.00179	180
Mid-plateau (t = 125 min)	55.1	400.0	47.9	14.2	33.7	0.864	43.2	18.662	0.01037	180
Plateau end / peak (t = 185 min)	71.4	400.0	62.4	20.4	42.0	1.226	61.3	37.577	0.02088	180

Late cooling (t = 335 min)	14.6	15.0	13.8	10.3	3.6	0.084	4.2	0.176	0.0000098	180

Table 1 consolidates the recorded and derived quantities at five representative points of the thermal cycle, read directly from the logged dataset underlying Figures 17–24.

The heat flow used as the denominator in Eq. (6), Q_{ref} = 180 W, is a fixed reference power adopted for all five operating points, not a per-point value measured or derived from the thermal-resistance model developed in Materials and Methods; as discussed below, the hot-side and cold-side branches of that model imply markedly different per-point heat flows that cannot yet be reconciled into a single value, so a fixed reference was preferred for this comparison. Accordingly, the derived quantity reported in the η (%) column throughout this study is a conversion ratio referred to this fixed reference power, and should not be read as a directly measured thermoelectric conversion efficiency.

- **Uncertainty analysis**

A brief propagation-of-uncertainty estimate was performed for the peak operating point (Plateau end, t = 185 min). The temperature-gradient uncertainty is dominated by the thermal camera's manufacturer-stated accuracy (±2 °C or ±2%, whichever is greater). Since $\Delta T = T_{hot} - T_{cold}$ is derived from two such independent readings, the combined uncertainty is $\Delta(\Delta T) = \sqrt{(\Delta T_{hot}^2 + \Delta T_{cold}^2)} \approx \pm 2.8$ °C, i.e., approximately ±7% of the peak ΔT ≈ 42.0 °C. The output voltage and current were measured with a manufacturer-stated accuracy of 0.7-4.0%, taking a representative mid-range value of ≈2%, the corresponding uncertainty at the peak point is $\Delta V_{out} \approx \pm 0.02$ V and ΔI ≈ ±1.2 mA. Propagating these through P = V·I gives $\Delta P/P = \sqrt{((\Delta V/V)^2 + (\Delta I/I)^2)} \approx \pm 2.8\%$, i.e., ΔP ≈ ±1.1 mW on the peak power of 37.6 mW. These figures should be read as indicative rather than a full metrological budget, since the campaign consisted of a single run and repeatability could not be independently assessed; a repeated campaign under similar conditions would be needed to establish the run-to-run (Type A) component of the uncertainty.

- **Extrapolating the results**

Based on the experimental results obtained using a limited number of thermoelectric modules, a theoretical scaling of the system was performed to estimate the potential electrical output when utilizing the entire available heated surface of the reactor door. The total surface area of the door is approximately 2178.75 cm^2, and excluding the handle area, it remains with a usable area of 2128.75 cm^2. Assuming the use of standard thermoelectric modules with approximate dimensions of 4 × 4 cm (16 cm^2 per module), the maximum number of modules that can be mounted is 133 modules. By extrapolation, the total theoretical electrical power becomes approximately 1.25 W. Such power levels are sufficient for several agricultural and autonomous applications, including powering wireless sensor nodes (soil moisture, temperature, humidity), supplying microcontrollers and data logging systems, charging small batteries or supercapacitors for intermittent operation and supporting low-power IoT communication modules, such as LoRa-based systems.

This extrapolated value of 1.25 W should be read as an upper-bound estimate rather than an expected operating point. It assumes a uniform temperature gradient across the entire 2128.75 cm^2 usable door surface, equal to the ΔT ≈ 42 °C measured at the single, most favorably located four-module array in the present setup, and a linear scaling of the cooling capacity of the cold-side heat sinks with the number of modules. In a real 133-module array, both assumptions would degrade: the temperature gradient is expected to be non-uniform across such a large surface, and the shared ambient air volume would reduce the effective convective heat-transfer coefficient per module as module density increases, so the true achievable output at that scale is expected to fall below this estimate.

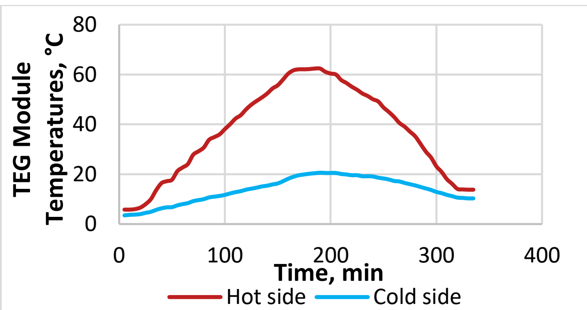

Fig. 17 - Temperatures of Peltier modules over time

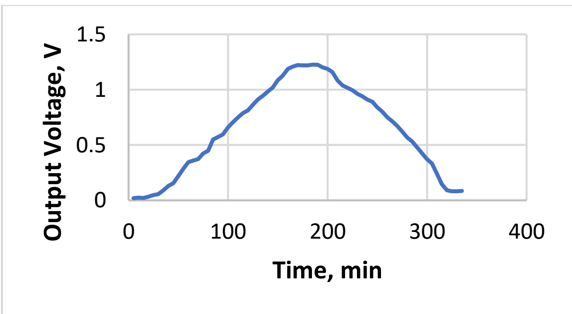

Fig. 18 - Output voltage over time

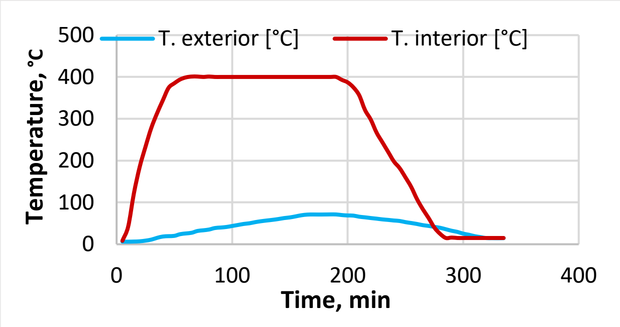

Fig. 19 - Heat source temperature over time

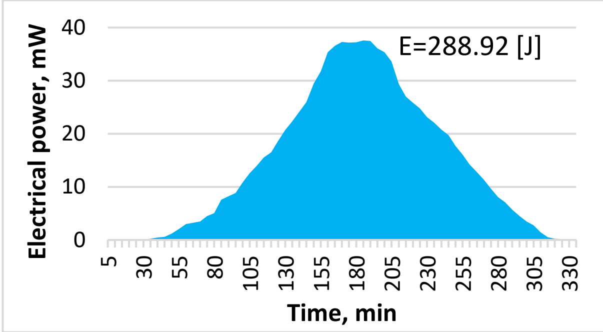

Fig. 20 - Electrical power over time

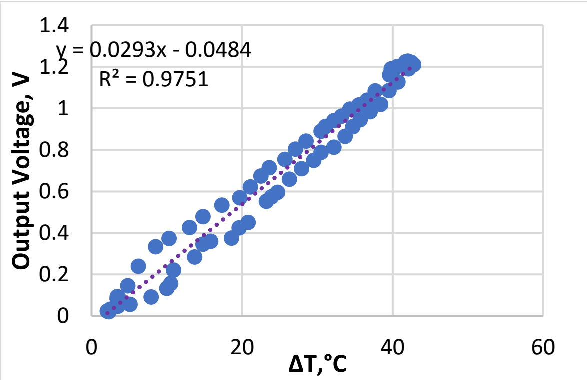

Fig. 21 - Dependence of Output Voltage on Temperature Gradient (ΔT)

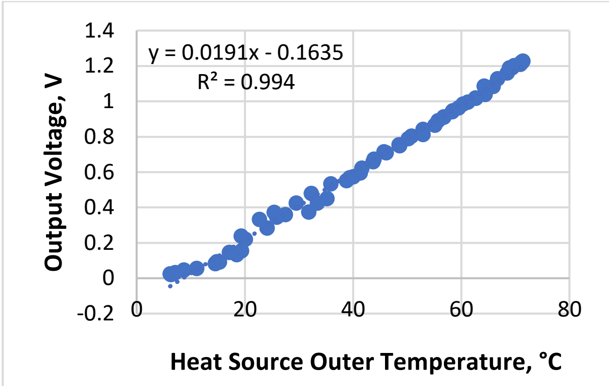

Fig. 22 - Dependence of Output Voltage on heat source outer temperature

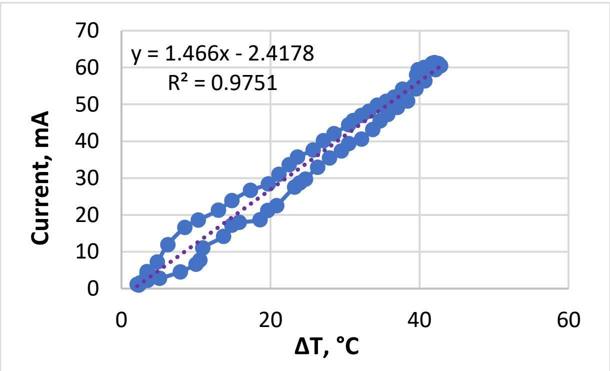

Fig. 23 - Dependence of Current on Temperature Gradient (ΔT)

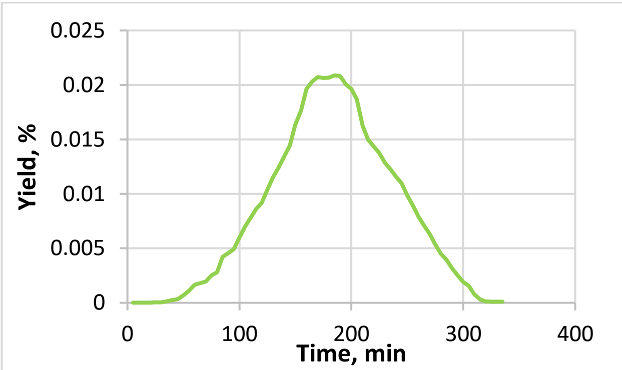

Fig. 24 - Dependence of Yield over time

DISCUSSION AND PERSPECTIVES

Despite the successful generation of electrical power, the overall P/Qref conversion ratio (yield) remained low, with a maximum value of approximately 0.021%. This limited value can be attributed to several factors, including:

- the relatively small temperature gradient across the modules compared to the high source temperature;
- thermal losses due to insufficient heat exchanger optimization;
- the intrinsic limitations of commercially available Peltier modules when used as thermoelectric generators.

Another significant limiting factor identified is the imperfect thermal contact between the heat source and the thermoelectric modules. This interface-related issue represents one of the primary causes of temperature loss in the system. Due to surface irregularities, non-uniform pressure distribution, and microscopic air gaps, a portion of the available thermal energy is not effectively transferred to the hot side of the Peltier modules. This phenomenon is inherently difficult to quantify experimentally, as it depends on contact quality at a micro-scale level, which cannot be directly measured with conventional instrumentation. As a result, it introduces uncertainty in the effective temperature gradient and reduces the overall system performance.

Furthermore, the data suggest that the external temperature of the heat source increased significantly more slowly than the internal temperature, indicating thermal resistance between the reactor core and the module interface. This highlights a critical design limitation and suggests that improved thermal coupling mechanisms, for example enhanced heat sinks, conductive interfaces, or forced cooling on the cold side could substantially increase ΔT and, consequently, electrical output.

One of the primary perspectives for improving system performance lies in the optimization of thermal coupling between the heat source and the thermoelectric modules. As identified in the present study, imperfect contact surfaces and intermediate layers introduce significant thermal resistance.

Future work should focus on:

- the use of advanced thermal interface materials with higher conductivity,
- improved mechanical fixation methods to ensure uniform pressure distribution,
- surface treatment techniques for example polishing or machining to reduce micro-scale air gaps; and the integration of phase-change materials to buffer transient thermal loads and stabilize the temperature gradient across the modules, as recently demonstrated for other TEG configurations (*Karadirek G. et al., 2025*).

The experimental results demonstrate that thermoelectric energy recovery from a biochar production system is feasible, albeit currently limited by low conversion efficiency and thermal losses. However, the obtained data also provide a solid basis for extrapolating the system performance under improved design and scaling conditions.

A key perspective for enhancing the overall electrical output lies in the geometric scalability of the thermoelectric system. In the present configuration, only a limited number of Peltier modules were installed. Considering the available surface of the reactor door, approximately 52.5 × 41.5 cm, excluding a 5 × 10 cm area occupied by the handle, a significantly larger number of modules could be mounted in a dense arrangement.

From a theoretical standpoint, increasing the number of modules proportionally increases the total electrical output, provided that similar thermal conditions (ΔT) are maintained. Under such conditions, the system could transition from milliwatt-level generation, tens of mW measured experimentally with four modules, toward the sub-2 W range estimated in this study for a full-door array of 133 modules (see the extrapolation above); reaching higher power levels would require a larger heated surface, a higher module density, or thermal management improvements beyond the present door-mounted geometry.

This scaling potential enables the consideration of practical applications within the agricultural sector, particularly for low-power and distributed systems. The generated energy could be used for:

- powering wireless environmental sensors, such as soil moisture, temperature, humidity;
- supplying data acquisition and transmission modules in precision agriculture systems;
- charging low-power batteries or supercapacitors for autonomous field devices;
- supporting IoT-based monitoring platforms integrated into biochar or biomass processing units.

Such applications are especially relevant in remote or off-grid agricultural environments, where energy autonomy and sustainability are critical.

An additional promising aspect identified in this study is the presence of secondary heated surfaces within the biochar equipment, reaching temperatures of up to approximately 250 °C. These areas represent an untapped thermal resource that could be exploited using specialized high-temperature thermoelectric modules (e.g., modules based on materials optimized for medium-to-high temperature gradients).

The integration of such modules could significantly increase the overall energy recovery potential of the system by:

- expanding the effective heat exchange surface,
- utilizing multiple thermal zones with different temperature levels,
- enabling a more efficient distribution of thermoelectric conversion across the equipment.

In a combined configuration—where both the reactor door and secondary heated surfaces are utilized—the system could evolve into a multi-source thermoelectric harvesting platform, substantially improving total electrical output and system viability.

Nevertheless, achieving these improvements requires addressing the limitations identified in the current study, particularly:

- reducing thermal contact resistance;
- optimizing heat transfer pathways;
- improving cold-side cooling efficiency.

Overall, while the present experimental setup yields relatively low electrical efficiency, the results clearly indicate that through scaling, improved thermal integration, and the use of advanced thermoelectric materials, biochar production systems have the potential to power low-consumption auxiliary electronics — such as wireless sensor nodes, data loggers, and IoT communication modules — rather than to serve as a primary energy source, given the very low P/Qref conversion ratio (~0.021%) obtained in this study. In this targeted, auxiliary-power role, the approach can still contribute to energy self-sufficiency and sustainability in agricultural applications.

CONCLUSIONS

This research demonstrates that thermoelectric energy recovery from a biochar production system is technically feasible: the surface-mounted TEG array reached a maximum output voltage of 1.226 V, a peak power of 37.6 mW, and a maximum temperature gradient of 42.8 °C over a 335-minute heating cycle, consistent with the expected Seebeck-effect behavior.

The overall P/Q_{ref} conversion ratio, referred to the fixed reference power Q_{ref} = 180 W rather than to a per-point modelled heat flow (see Results), nonetheless remained very low (maximum ≈ 0.021%), driven primarily by imperfect thermal contact between the heat source and the module hot side and by the intrinsic limitations of Peltier modules repurposed as generators, as discussed above.

Scaling to the full reactor-door surface indicates that a multi-module array could reach power levels sufficient for low-consumption auxiliary electronics — wireless sensor nodes, data loggers, and IoT communication modules — though not for primary power generation.

Taken together, these results position TEG-based waste heat recovery from biochar production as a viable auxiliary-power source for agricultural monitoring applications, contributing to energy self-sufficiency in a targeted, realistic role rather than as a primary generation method.

ACKNOWLEDGEMENT

This paper was supported by the NUCLEU Program, through Project 9N/ 01.01.2023, "Technology for the valuation of vegetable residues in the form of biochar for the improvement of soil quality," carried out with the support of ANCSI.

REFERENCES

[1] Badaka, H. K., & Morega, A. M. (2024). Simulation of biomass carbonization and heat recovery for electricity production using Seebeck modules. *Revue Roumaine des Sciences Techniques – Série Électrotechnique et Énergétique*. https://doi.org/10.59277/RRST-EE.2024.69.3.17

[2] Champier, D. (2017). Thermoelectric generators: A review of applications. *Energy Conversion and Management, 140, 167–181*. https://doi.org/10.1016/j.enconman.2017.02.070

[3] Chelladorai, P., Atekov, P., Balakrishnan, N., Kashyap, A., Chakravarty, P., & Naresh, G. (2024). Computational and Experimental Evaluation of Thermoelectric Generator for Waste Heat Recovery in Internal Combustion Engine Applications. *SAE Technical Paper 2024-01-5076*.

[4] Ciupercă, R., Constantin, A.-M., Zaica, A., & Ștefan, V. (2022). Recovery of solar thermal energy and energy from the composting process. *INMATEH – Agricultural Engineering, 68*(3), 896–905. https://doi.org/10.35633/inmateh-68-89

[5] Cui, X., Chen, X., & Gao, Z. (2024). Research on the power generation performance and optimization of thermoelectric generators for recycling remaining cold energy. *Energy, 299, 131422*. https://doi.org/10.1016/j.energy.2024.131422

[6] Deng, Y., Liu, X., & Su, C. (2022). Experimental investigation of thermoelectric generator for waste heat recovery from biomass combustion systems. *Renewable Energy, 189*, 1234–1243. https://doi.org/10.1016/j.renene.2022.03.045

[7] Hqgraphene, available online: https://www.hqgraphene.com/Bi2Te3.php Bi2Te3 – Bismuth Telluride (product page). Accessed August 2026.

[8] Iavnic, T., Puiu, D., & Popescu, A. (2024). Energy recovery from waste heat using thermoelectric generators. *Buletinul Institutului Politehnic din Iași, 69*(4), 21–35. https://doi.org/10.2478/bipcm-2023-0032

[9] Jiang, Y., Wang, Y., Yan, J., Shen, L., & Qin, J. (2024). Research on the performance of thermoelectric self-powered systems for wireless sensors based on industrial waste heat. *Sensors, 24(18), 5983*, MDPI. https://doi.org/10.3390/s24185983

[10] Karadirek, G., Taylan, G., Baykara, T., & Helvacı, H. U. (2025). Experimental performance evaluation of phase change material integrated thermoelectric generator. *International Journal of Energy Studies, 10(3), 963–981*. https://doi.org/10.58559/ijes.1686912

[11] Liu, Z., Zhang, H., & Wang, X. (2023). Performance analysis of thermoelectric generators for low-grade waste heat recovery: A review. *Energy Conversion and Management, 278, 116657*. https://doi.org/10.1016/j.enconman.2023.116657

[12] Maican, E. (2015). Renewable energy systems / Sisteme de energii regenerabile, *Printech Publishing House*, Bucharest/Romania

[13] Mastrullo, R., Mauro, A. W., & Vanoli, G. P. (2019). Thermoelectric generators for energy recovery from industrial processes: A review. *Energy Procedia, 158*, 120–125. https://doi.org/10.1016/j.egypro.2019.01.062

[14] Kim, M., Park, D., & Kim, J. (2025). A review on recent selenium- and tellurium-based thermoelectric materials and chalcogenide/organic flexible thermoelectric applications. *Materials Chemistry and Physics, Volume 337*, 1 June 2025, 130571. https://doi.org/10.1016/j.matchemphys.2025.130571

[15] Moriarty, P., & Honnery, D. (2016). Can renewable energy power the future? *Energy Policy, Vol. 93*, pp. 3-7, ISSN 0301-4215

[16] Ridwan, M. (2025). Principle and applications of thermoelectric generators: A review. *Sensors, 25(8), 2484*. https://doi.org/10.3390/s25082484

[17] Quan, R., Li, T., Yue, Y., Chang, Y., & Tan, B. (2020). Experimental study on a thermoelectric generator for industrial waste heat recovery based on a hexagonal heat exchanger. *Energies, 13(12), 3137*, MDPI. https://doi.org/10.3390/en13123137

[18] Sanin-Villa, D. (2022). Recent developments in thermoelectric generation: A review. *Sustainability, 14(24), 16821*, MDPI. https://doi.org/10.3390/su142416821

[19] Săvescu, C., Morega, A. M., Roman, M., & Nechifor, C. (2025). Experimentally validated studies of thermoelectric generators installed on a compressor test bench. *Revue Roumaine des Sciences Techniques – Série Électrotechnique et Énergétique*. https://doi.org/10.59277/RRST-EE.2025.2.7

[20] Wang, Y., Wang, R., Chai, R., Ding, R., Ye, Q., Sun, Z., Meng, X., & Sun, D. (2025). Review of automotive thermoelectric generator structure design and optimization for performance enhancement. *Processes, 13(6), 1931*. https://doi.org/10.3390/pr13061931

[21] Weatherspark. Historical Weather on December 11, 2025 in Bucharest, Romania. Accessed August 2026. Available online: https://weatherspark.com/h/d/93241/2025/12/11/Historical-Weather-on-Thursday-December-11-2025-in-Bucharest-Romania#Figures-Temperature

[22] Williams, N. P., Power, J., Trimble, D., & O'Shaughnessy, S. M. (2022). An experimental evaluation of thermoelectric generator performance under cyclic heating regimes. *Heat and Mass Transfer, 60*, 1991–2003. https://doi.org/10.1007/s00231-022-03280-5

[23] Yaman, K., Dölek, S., & Arslan, G. (2025). Performance analysis of a thermoelectric generator (TEG) for waste heat recovery. *WAPRIME, 2(1), 13–20*. https://doi.org/10.5281/zenodo.16980562